



A disposable acoustofluidic chip for nano/micro particle separation using unidirectional acoustic transducers

Journal:	<i>Lab on a Chip</i>
Manuscript ID	LC-ART-01-2020-000106.R1
Article Type:	Paper
Date Submitted by the Author:	06-Mar-2020
Complete List of Authors:	<p>Zhao, Shuaiguo; Duke University, Mechanical Engineering and Materials Science Wu, Mengxi; University of Michigan, Mechanical Engineering Yang, Shujie; Duke University, Mechanical Engineering and Materials Science Wu, Yuqi; Duke University Gu, Yuyang; Duke University, MEMS Chen, Chuyi; Duke University, Mechanical Engineering and Materials Science Ye, Jennifer; Duke University, Mechanical Engineering and Materials Science Xie, Zhemiao; Duke University, MEMS Tian, Zhenhua; Duke University, Mechanical Engineering and Materials Science Bachman, Hunter; Duke University, MEMS Huang, Po-Hsun; Duke University, Mechanical Engineering and Material Sciences Xia, Jianping; Duke University, Mechanical Engineering and Materials Science Zhang, Steven Peiran; Duke University, Mechanical Engineering and Materials Science Zhang, Heying; Duke University, Mechanical Engineering and Materials Science Huang, Tony; Duke University, Mechanical Engineering and Materials Science</p>



Journal Name

ARTICLE

A disposable acoustofluidic chip for nano/micro particle separation using unidirectional acoustic transducers

Shuaiguo Zhao, Mengxi Wu, Shujie Yang, Yuqi Wu, Yuyang Gu, Chuyi Chen, Jennifer Ye, Zhemiao Xie, Zhenhua Tian, Hunter Bachman, Po-Hsun Huang, Jianping Xia, Peiran Zhang, Heying Zhang, and Tony Jun Huang*

Received 00th January 20xx,
Accepted 00th January 20xx

DOI: 10.1039/x0xx00000x

www.rsc.org/

Separation of nano/micro particles based on surface acoustic waves (SAWs) has shown great promise for biological, chemical, and medical applications ranging from sample purification to cancer diagnosis. However, the permanent bonding of a microchannel onto relatively expensive piezoelectric substrates and excitation transducers renders the SAW separation devices non-disposable. This limitation not only requires cumbersome cleaning and increased labor and material costs, but also leads to cross-contamination, preventing its implementation in many biological, chemical, and medical applications. Here, we demonstrate a high-performance, disposable acoustofluidic platform for nano/micro particle separation. Leveraging unidirectional interdigital transducers (IDT), a hybrid channel design with hard/soft materials, and the tilted-angle standing SAW (taSSAW), our disposable acoustofluidic devices achieve acoustic radiation forces comparable to those generated by existing permanently bonded, non-disposable devices. Our disposable devices can separate not only microparticles but also nanoparticles. Moreover, it can differentiate bacteria from human red blood cells (RBCs) with a purity of up to 96%. Altogether, we developed a unidirectional IDT-based, disposable acoustofluidic platform for micro/nano particle separation that can achieve high separation efficiency, versatility, and biocompatibility.

Introduction

Separation of nano to microscale particles such as exosomes,^{1, 2} bacteria,³⁻⁵ and cells^{6, 7} is of great interest in a variety of assays from fundamental biological studies to medical applications, including drug screening, disease diagnosis, and cell biology.⁸⁻¹⁰ Towards the goal of separating bioparticles with high purity, yield, versatility, and biocompatibility, researchers are continuously developing new separation technologies by introducing a variety of physical principles, such as magnetophoresis,⁷ dielectrophoresis,¹¹ acoustofluidics,¹² hydrodynamics,¹³ and photophoresis.¹⁴ Amongst these physical principles, surface acoustic wave (SAW)-based separation has recently emerged as a promising technology, because it does not require labelling of target particles/cells,^{12, 15, 16} uses relatively low electrical power,^{12, 17} and has high precision and versatility.¹⁷⁻²⁶ With these advantages, SAW-based devices^{2, 6, 16, 22, 27-33} have shown outstanding potential for separating microvesicles from red blood cells (RBCs),²⁹ exosomes from whole human blood,² human breast cancer cells from leukocytes,⁶ and bacteria from peripheral blood mononuclear cells.³

Ideally, the SAW separation chips should be conveniently replaced and disposed. Disposable chips will help supply a sterile system, eliminate sample cross-talk, and facilitate simple maintenance. However, in most SAW separation chips, the microfluidic chamber is permanently bonded onto a piezoelectric

substrate and excitation transducers. Since the piezoelectric substrate and excitation transducers are often too expensive to be disposed, this limitation necessitates cumbersome cleaning processes and can induce cross-contamination, especially for biological and clinical samples. Therefore, it is important to develop disposable SAW chips in which the microfluidic cartridges can be separated from the piezoelectric substrate and excitation piezoelectric transducers. Thus, only the microfluidic cartridges are disposable, while the piezoelectric substrate and excitation piezoelectric transducers are reusable. To date, disposable SAW devices have been introduced into different scenarios due to their significance for real-world applications. Examples include droplet splitting³⁴ and sorting,^{16, 35, 36} and particle pattern,^{37, 38} deflection,²⁸ and separation.³⁹ For separation, Ma *et al.* separated 15 μm polystyrene (PS) particles from 10 μm PS particles in a disposable microchannel with polydimethylsiloxane (PDMS) post using traveling SAWs.³⁹ Despite these progressions, the performance of the currently demonstrated disposable SAW devices are not as good as the permanently bonded SAW devices. For example, nanoparticle separation or cell separation using a disposable SAW device has not been demonstrated. This is likely due to the weak acoustic energy in disposable SAW devices.

In this work, we present a unidirectional interdigital transducers (IDTs) based, tilted-angle standing SAW (taSSAW) chip for high-performance separation of nano-to-micro sized particles in a continuous flow. To effectively transmit acoustic energy into our disposable acoustofluidic (*i.e.*, the fusion of acoustics and microfluidics)^{33, 39-57} devices, a hybrid hard/soft polydimethylsiloxane (PDMS) microchannel was designed. The hard PDMS, which is

Department of Mechanical Engineering and Materials Science, Duke University, Durham, NC 27708, USA. E-mail: tony.huang@duke.edu
Electronic Supplementary Information (ESI) available. See DOI: 10.1039/x0xx00000x

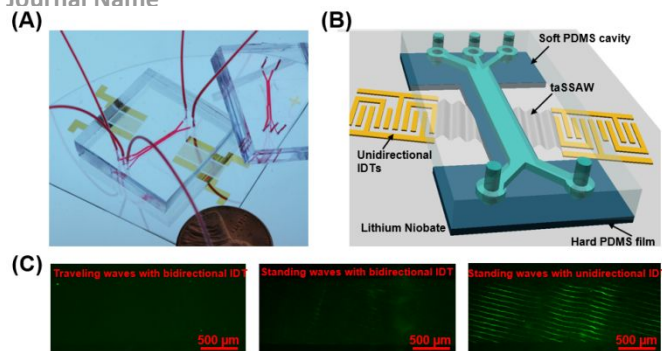


Fig. 1 (A) Photograph and (B) schematic for the disposable acoustofluidic separation chip using unidirectional IDT based taSSAW design. (C) Patterning of 400 nm PS particles within disposable hard/soft microchannels with a 13 μm hard PDMS film at 20 V_{pp} using traveling waves with a bidirectional IDT design (left), standing waves with a bidirectional IDT design (middle), and standing waves with a unidirectional IDT design (right), respectively. For all these three designs, disposable microchannels were placed on SAW substrates with a relative orientation of 15° to IDT for comparison.

different from the commonly used soft PDMS^{58, 59}, has a low acoustic attenuation coefficient^{60, 61} and can be fabricated as an ultra-thin PDMS film, enabling the increase of acoustic pressure in disposable microchannels. As a result, the intensity of acoustic radiation force achieved in our disposable acoustofluidic device is comparable to that in permanently bonded devices. Four different sized particles were precisely deflected into separate and distinguishable streams, indicating its accuracy and versatility. We have achieved separation of different particles with a wide size range from 200 nm to 10 μm in a single device, including the separation of 2 and 4.5 μm polystyrene (PS) particles, 110 nm PS and 1 μm PS particles, 400 nm PS and 660 nm silicon dioxide (SiO_2) particles, and 100 nm PS and 200 nm Silver (Ag) particles. Additionally, our disposable device showed a separation purity of up to 96% when separating *Escherichia coli* (*E. coli*) from human RBCs.

Compared to previous reported disposable acoustofluidic devices that use travelling SAW or standing SAW with bidirectional IDT designs,^{16, 28, 34, 38, 39} our taSSAW device generated with a unidirectional IDT design has the advantage of generating a stronger acoustic field and achieving a larger separation displacement (distance variation between two types of particles in the direction perpendicular to fluid flow). This advantage is achieved by the unidirectional IDT design, the taSSAW design, and the hybrid hard/soft PDMS microchannel. Our unidirectional IDT based taSSAW device drives particles using a strong, periodic acoustic radiation force. With strong acoustic gradients and large separation displacements, our disposable acoustofluidic chip is capable of precisely separating not only microparticles but also nanoparticles. In contrast, the existing disposable acoustofluidic devices can only manipulate large micro-objects.^{28, 38, 39} Our chip is also the first disposable acoustofluidic device that demonstrates separation of biological cells. With its advantages of being versatile, precise, label-free, and low-cost, we believe that our unidirectional IDT based disposable devices can facilitate the development of acoustofluidic technologies into point-of-care systems.

Materials and Methods

Device fabrication

As shown in Fig. 1, the unidirectional IDT based disposable acoustofluidic chip consists of a reusable SAW transducer and a disposable microchannel. To fabricate a reusable SAW transducer, a 128° Y-cut X-propagation LiNbO_3 (PWLN-431232, Pmoptics, USA) wafer was chosen as the piezoelectric substrate. A set of 80 pairs of unidirectional IDTs were patterned onto the LiNbO_3 using photolithography, followed by a deposition of Cr (50 \AA) and Au (500 \AA) through e-beam evaporation (CHA Industries, USA). After a lift-off process, IDTs were obtained with a feature size of 10 μm and a wavelength of 120 μm , corresponding to a resonance frequency of 33.13 MHz.

In Fig. 1B, the disposable microchannel was fabricated by bonding the top soft PDMS cavity to the bottom Gelest hard PDMS film. The top PDMS cavity with 800 μm width and 75 μm depth was obtained by standard soft-lithography. Briefly, after obtaining an SU-8 mold, a 10:1 mixture of soft PDMS base and curing agent (Sylgard184 Silicone Elastomer Clear, Ellsworth, USA) was degassed, poured onto the mold, cured for 1 h and peeled off. To fabricate the Gelest hard PDMS film, a 1:1 mixture of PDMS base and curing agent (PP2-RG07, Gelest, Inc., USA) was spin-coated on a clean silicon wafer via a spin coater (WS-650MZ-23NPPB, Laurell Inc., USA) and partially cured at 65 $^\circ\text{C}$ for 20 min. Gelest hard PDMS is a different composite material relative to Sylgard 184 PDMS, and has not been applied in acoustofluidic devices previously. The hardness was measured as 8.62 MPa for Gelest hard PDMS, and 4.11 MPa for Sylgard soft PDMS using nanoindenter (Hysitron Ubi-1, USA). The acoustic attenuation coefficient and speed of sound in Gelest hard PDMS and Sylgard soft PDMS were also measured (Fig. S1 in the Supporting Information). Then, this Gelest hard PDMS film was bonded with the Sylgard soft PDMS cavity and baked at 65 $^\circ\text{C}$ overnight. During this process, the soft PDMS cavity was treated with oxygen plasma to enhance its bonding strength with the Gelest hard PDMS film. Finally, with van der Waals forces induced self-adhesion, the disposable microchannel was gently pressed and attached to a SAW substrate at a relative orientation of 15° through markers on LiNbO_3 , forming a disposable acoustofluidic chip.

For the comparison of different disposable acoustofluidic devices, disposable microchannels with different types of PDMS film were fabricated, including $13 \pm 0.8 \mu\text{m}$ (2,200 rpm/min for 3 mins) and $20 \pm 1.5 \mu\text{m}$ (1,500 rpm/min for 3 mins) Sylgard soft PDMS films, and $13 \pm 0.5 \mu\text{m}$ (1,500 rpm/min for 3 mins) and $20 \pm 1 \mu\text{m}$ (1,000 rpm/min for 3 mins) Gelest hard PDMS films. Gelest hard PDMS curing agent and base were mixed at a ratio of 1:1, while soft Sylgard PDMS curing agent and base were mixed at 1:10. Note that attempts have been made but failed in fabricating a PDMS film at a mixing ratio of 1:1 using Sylgard 184 PDMS (Fig. S2 in the Supporting Information). The thickness of PDMS films was measured using a profilometer (Dektak 150, Bruker, USA). These different disposable PDMS channels were then assembled on the same IDT substrate, respectively. For the comparison of non-disposable and disposable acoustofluidic devices, the same IDT substrate is then permanently bonded with soft PDMS cavity through oxygen plasma treatment, to fabricate non-disposable acoustofluidic devices. For clarification, the Gelest hard PDMS and Sylgard soft PDMS will be referred as "hard PDMS" and "soft PDMS" in the later sections.

Experimental setup

Different PS particles included non-fluorescent PS particles (10 μm , 6 μm , 4.5 μm , and 1 μm Polysciences, USA), green fluorescent PS particles (2.0 μm , 1.0 μm , 400 nm, and 110 nm, Bangs Laboratories, USA), Ag nanoparticles (200 nm, 796360, Sigma-Aldrich, USA) and SiO₂ nanoparticles (660 nm, Fig. S3 in the Supporting Information) were suspended in DI water containing 0.5 % sodium dodecyl sulfate (SDS) as samples. To prepare the mixture of bacteria and RBCs, *E. coli* (8739, ATCC, USA) was cultured in a sterilized Miller's LB Broth medium (20716002, Cellgro, USA), and then stained with a BacLight kit (L7007, Invitrogen, USA). After that, 3 μL of RBCs (SER-10MLRBC, Zen-Bio, USA) and 20 μL of cultured *E. coli* were mixed in 1 mL PBS filtered with a 0.2 μm filter (514-0072, VWR, USA). The final concentration for RBCs was calculated as approximately 1.1×10^7 particles/mL using a hemocytometer, and that for *E. coli* was measured as approximately 5.0×10^6 particles/mL via a microreader (BioTek, USA). Before experiments, all the microchannels were treated with 1% bovine serum albumin (Sigma-Aldrich, USA) solution for 5 min to prevent the adsorption of particles on microchannel.

During all the measurements, SAW devices were driven by a function generator (E4422B, Agilent, USA) and an amplifier (25A250A, Amplifier Research, USA). The targeted sample and sheath fluids were injected into microchannel inlets by a syringe pump (neMESYS, Cetoni GmbH, Germany). The flow rate of sample and two sheath fluids were set as 2, 2, and 6 $\mu\text{L}/\text{min}$, respectively, for particle and bacteria separation unless otherwise stated, while they were 0.3, 10, and 10 $\mu\text{L}/\text{min}$, respectively, for hydrodynamic focusing. For particle deflection and separation, and bacteria separation, SAW devices were placed on a Peltier cooling system (TEC1-12730, Hebei I.T., China) and experimental processes were monitored with a charge-coupled device (CCD) (CoolSNAP HQ2, Photometrics, USA) on an upright microscope (BX51W1, Olympus, Japan). For particle velocity test, the processes of particle patterning at different input voltages were recorded with a high-speed camera (500K-M1, Photron, Japan) on an inverted microscope (Eclipse Ti, Nikon, Japan) and analyzed using ImageJ (NIH, USA). Separated samples were collected from two microchannel outlets with 1.5 mL microtubes (8081811, Sarstedt, Germany).

Sample characterization

In order to provide a benchmark comparison for our acoustofluidic devices, SEM and flow cytometry were applied to analyze separation performance. For SEM imaging, separated particles were dropped on a clean silicon wafer, dried in a chemical hood, sputtered with gold, and then observed with an electron microscope (FEI XL30, FEI, USA). For flow cytometry, 50 μL of mixed *E. coli* and RBCs, separated *E. coli*, and separated RBCs were diluted with 1 mL PBS in a 5 mL tube (352235, Falcon, USA), respectively. After that, the samples were tested by a flow cytometer (BD FACSCanto B, USA) and analyzed using FlowJo software (FlowJo, FlowJo, LLC, USA).

Results and discussion

Characterization of disposable acoustofluidic chips with hybrid hard/soft material design

To develop a disposable acoustofluidic chip for bioparticle separation, we introduce taSSAWs generated by unidirectional IDTs

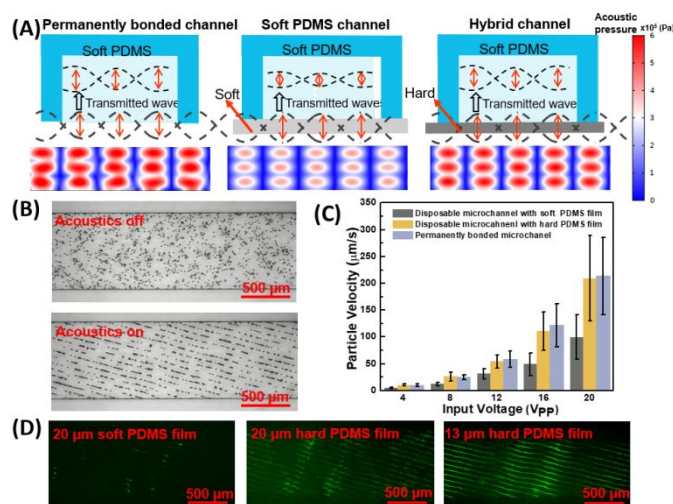


Fig. 2 The performance of disposable acoustofluidic chips in the absence of fluid flow. (A) Schematic illustrations and corresponding numerical simulations for permanent bonded channel, disposable soft microchannel with a 20 μm soft PDMS film, and disposable hybrid hard/soft channel with a 13 μm hard PDMS film illustrate the influence of coupling layer in acoustic pressure transmission. (B) Patterning of 10 μm PS particles in a disposable acoustofluidic device with a hybrid hard/soft PDMS channel. (C) Quantitative performance comparison of a permanently bonded acoustofluidic device to a disposable device by measuring 10 μm particle velocity during their patterning at different input voltages. (D) Comparison of the taSSAW field by patterning 400 nm PS particle in a disposable channel with a 20 μm soft PDMS film (left), a 20 μm hard PDMS film (middle), and a 13 μm hard PDMS film (right).

into a disposable PDMS microchannel. Figs. 1A and B illustrate the concept and working mechanism for the disposable acoustofluidic chip, which consists of a reusable SAW substrate and a disposable PDMS microchannel. The SAW substrate is a LiNbO₃ patterned with a pair of parallel unidirectional distributed IDTs (Fig. S4 in the Supporting Information) to address the weak acoustic energy generated in disposable microchannels. In Fig. S5 in the Supporting Information, the unidirectional IDT proves to have a much larger transmission energy of S₂₁ in the “toward” configuration relative to the “away” configuration, while bidirectional IDT has almost equivalent S₂₁ in “toward” and “away” configurations, demonstrating the directionality of our unidirectional IDTs. Specifically, the peak value of S₂₁ for unidirectional IDTs is *ca.* -5 dBm while it is *ca.* -11.2 dBm for bidirectional IDTs, indicating that under the same experimental conditions, unidirectional IDTs can generate SAWs with higher vibrational amplitudes than traditional bidirectional IDTs. The disposable microchannel has a soft PDMS cavity enclosed by a hard PDMS film. Under the Van der Waals forces induced self-adhesion,^{34, 62} the closed, disposable microchannel was assembled between IDTs on the LiNbO₃ at an orientation of 15° relative to IDTs. When the IDTs are activated, two identical and opposing traveling SAWs would be generated, and propagate along the surface of the LiNbO₃. These traveling SAWs constructively interfere with each other and form a standing SAW. Such a standing SAW generates parallel pressure nodal lines at the specific angle of 15° with respect to the disposable microchannel, termed as “taSSAW” (Fig. 1B). This taSSAW transmits through the hard PDMS film and couples into disposable microchannels. Once transmitted taSSAWs meet with particles, acoustic radiation force would be exerted on particles toward the pressure nodal lines.^{63, 64} With

particle patterning, we further compared traveling waves with a bidirectional IDT design, standing waves with a bidirectional IDT design, and standing waves with a unidirectional IDT design in Fig. 1C. The results demonstrate that standing waves with a unidirectional IDT design can generate much stronger acoustic field and larger acoustic radiation force on particles than the other two designs.

Different particles with different intrinsic physical properties (such as size, density, and compressibility) would experience differential acoustic radiation forces and move differently in the microfluidic channel. This discrepancy in movement can be leveraged to achieve micro/nano particle separation. Meanwhile, as the pressure nodal lines lie across the whole disposable microchannel at the angle of 15° , the separation displacement would be much larger than the acoustic wavelength. Once finished with a given acoustic separation test, the disposable microchannel can be easily replaced by peeling off the used PDMS-based microfluidic channel and aligning a clean microchannel assembly to the same SAW substrate. Hence, our devices can avoid cross-contamination; meanwhile, they can significantly reduce the average cost for multiple tests, since only the low-price PDMS channel needs to be replaced, while the expensive LiNbO_3 substrate and excitation piezoelectric transducers are reusable.

The performance of the disposable acoustofluidic device is related to the transmitted taSSAW in closed, disposable microchannels, which generates acoustic radiation force on particles/cells. The acoustic radiation forces are proportional to the square of acoustic pressure.⁸ To enhance the acoustic pressure within the disposable microchannel, we employed a hybrid hard/soft PDMS channel to enhance the acoustic transmission. In particular, we bonded a Sylgard soft PDMS cavity onto a $13\ \mu\text{m}$ Gelest hard PDMS film (Fig. 2A). For comparison, the soft PDMS channel in Fig. 2A has a thickness of $20\ \mu\text{m}$ due to fabrication limitation (Fig. S6 in the Supporting Information). Gelest hard PDMS has a much smaller acoustic attenuation coefficient ($\approx 4432\ \text{dB/m}$) than Sylgard soft PDMS ($\approx 23798\ \text{dB/m}$), which can reduce acoustic attenuation in PDMS film (Table 1 in the Supporting Information). Additionally, the larger acoustic impedance of Gelest hard PDMS ($\approx 1.13\ \text{MPa}\cdot\text{s/m}$) compared to Sylgard soft PDMS ($\approx 0.96\ \text{MPa}\cdot\text{s/m}$) enables a smaller impedance mismatch between water ($\approx 1.49\ \text{MPa}\cdot\text{s/m}$) and PDMS film, enhancing acoustic transmission (Table 1 in the Supporting Information). Thus, whereas 61.9% of the acoustic pressure is transmitted into soft PDMS channel, the transmitted acoustic pressure is increased to 92.1% in the new hybrid hard/soft PDMS channel (Numerical simulation in Fig. 2A). When compared to a permanently bonded device, the magnitude of the acoustic radiation force is only reduced by 15.2% within the disposable device using the hybrid hard/soft PDMS channel, whereas the radiation force is reduced by 61.7% within the disposable device using the soft PDMS channel. With this larger acoustic radiation forces, our disposable device using the hybrid hard/soft PDMS channel would improve its capability to manipulate small particles.

We next quantitatively analyzed the taSSAW acoustic field in permanently bonded devices and disposable devices by calculating particle velocity during manipulation. In Fig. 2B, when the taSSAW was applied, $10\ \mu\text{m}$ PS particles were patterned homogeneously and periodically along the pressure nodes, indicating uniformly coupled

acoustic waves. We have also observed diffractive effects within both disposable microchannels and permanent bonded channels,⁶⁵ which do not adversely affect the particle separation process. During this acoustic patterning process, particles were subjected to an acoustic radiation force, which aligned particles from random dispersion to pressure nodes; as such, the particle velocity provides an indication of the acoustic radiation force.³⁷ The quantitative characterization of $10\ \mu\text{m}$ PS particle velocities during their patterning is given in Fig. 2C. To ensure accuracy, disposable microchannels with different PDMS films and permanent microchannel were attached on the same SAW substrate. To check the variability between experiments, we measured the particle velocities of four different disposable hybrid channels on the same SAW substrate at $20\ V_{\text{pp}}$ (28.2 dBm). The results from these experiments yielded an average velocity of $202 \pm 16.3\ \mu\text{m/s}$ (\pm one standard deviation), demonstrating the consistency of our disposable acoustofluidic devices (Fig. S7 in the Supporting Information). In comparison with the commonly used, permanently bonded device, the results indicate a 43% to 55% loss of particle velocity when using the disposable device with a soft PDMS bottom film, but only a 2% to 10% loss for our devices with a hybrid hard/soft PDMS across varying input voltages from 4 to $20\ V_{\text{pp}}$ (14.2 to 28.2 dBm). Based on the numerical simulations in Fig. 2A, the numerical loss difference between disposable devices using the hybrid channel and soft channel is approximately 46.5%, which matches well with the experimental difference (41%–45%). Note that a small mismatch (*c.a.* 10%) exists between the experimental and numerical calculation of the acoustic radiation force discrepancy for disposable devices, which can be attributed to the deviation in the calculation of the acoustic attenuation coefficient. To further examine the influence of the coupling layer on taSSAW field, $400\ \text{nm}$ PS particles were patterned using disposable devices with different PDMS film (Fig. 2D). Clearly, nanoparticles were patterned periodically along the tilted-angle direction via the transmitted taSSAW on both hybrid hard PDMS channels, even with a thickness of $20\ \mu\text{m}$. With its larger acoustic radiation force, our disposable device has a much greater capability for manipulating small particles. Overall, these results imply that the intensity of acoustic waves generated in our disposable devices is comparable to that in commonly used, permanently bonded devices.

Compared to the reported 85% to 90% loss of particle velocity in previous disposable devices,^{16, 35–39} which cannot be used to separate nanoparticles, the significant improvement in our disposable acoustofluidic device can be attributed to the following reasons. First, the taSSAW generated by unidirectional IDTs provides a strong acoustic field. Second, in our hybrid hard/soft microchannel design, hard PDMS has a much smaller acoustic attenuation coefficient, larger acoustic impedance, and a smaller film thickness than commonly used soft PDMS, which significantly improves acoustic energy transmission.

Disposable acoustofluidic chips for particle deflection

Separation of bioparticles results from discrepancies in their deflections. Using our disposable acoustofluidic devices, we analyzed the relative deflection displacement of particles before conducting particle-separation experiments. Fig. 3 shows the dependence of

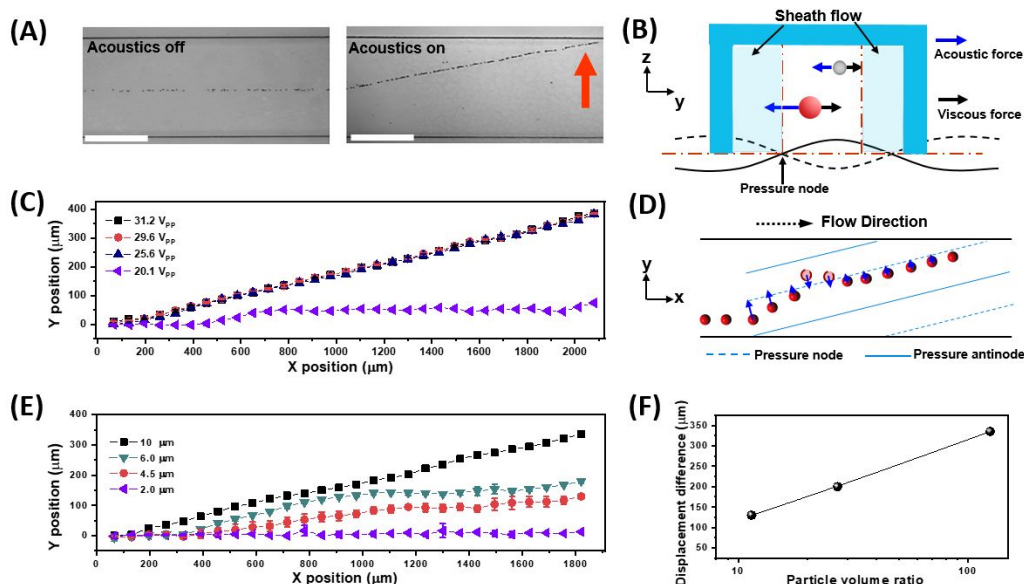


Fig. 3 Disposable acoustofluidic chips for particle deflection in a continuous flow. (A) Trajectories of 6 μm PS particles with and without taSSAW acoustic field. Scar bar: 500 μm . The red arrow represents the direction of particle deflection, which is consistent with the entire article. (B) Trajectories of 6 μm PS particles at different acoustic intensities. (C) Trajectories of 10, 6, 4.5, and 2.0 μm PS particles at the same acoustic intensity. (D) Schematic for particle position adjacent to pressure node. (E) Schematic of size-based particle deflection with respect to net forces. (F) The relationship between displacement difference and particle volume ratio.

measured particle deflection on acoustic intensity and particle size. To ensure measurement accuracy, three-inlet hydrodynamic focusing was applied, allowing particles to enter consistently into the same position in the acoustic field. As shown in Fig. 3A, when the taSSAW was not applied, particles flowed through the microchannel in a single stream. Once the taSSAW was applied, particles were deflected along the pressure node line. The deflection of the particles are determined by the acoustic radiation force (F_r), which pushes particles toward pressure nodal lines, and the Stokes drag force (F_d), which hinders the motion of particles⁸ (Fig. 3B). These two forces can be expressed as follows:

$$F_r = -\left(\frac{\pi p_0^2 v \beta_f}{2\lambda}\right) \phi \sin(2kL) \quad (1)$$

$$F_d = -6\pi\eta r v \quad (2)$$

$$\phi(\beta, \rho) = \frac{5\rho_p - 2\rho_f}{2\rho_p + \rho_f} - \frac{\beta_p}{\beta_f} \quad (3)$$

where p_0 , λ , ϕ , k , and L represent acoustic pressure amplitude, acoustic wavelength, acoustic contrast factor, acoustic wavenumber, and the distance from particle position to the pressure node, respectively, and β_f , η , and ρ_f are the compressibility, viscosity, and density of fluid, respectively. β_p , ρ_p , v , T , and v are the compressibility, density, volume, radius of particles, and the relative velocity of particle to fluid, respectively. Among these parameters, the acoustic contrast factor ϕ determines the direction of acoustic radiation force. PS particles have positive ϕ (0.437), and therefore were deflected to pressure nodes.

Fig. 3C displays the influence of acoustic intensity on the deflection distances (distance of migration of one type of particles in the direction perpendicular to fluid flow) of 6 μm PS particles. With increasing voltage from 20.1 to 31.2 V_{pp} (28.6 to 32 dBm), the extent of particle deflection first increases, and then remains unchanged. Fig. S8A in the Supporting Information shows the raw image data. According to Equation (1), the increase in drive voltage from 20.1 to

25.6 V_{pp} (28.6 to 30.3 dBm) increases the acoustic radiation force and therefore the net force. In this way, particles at 25.6 V_{pp} (30.3 dBm) would move closer to the tilted-angle pressure node. With a further increase in the drive voltage from 25.6 to 31.2 V_{pp} (30.3 to 32 dBm), particles remained at positions adjacent to pressure node, and cannot pass through the pressure node. Otherwise, the strong acoustic radiation force would drive particles back to pressure node quickly (Fig. 3D). In other words, the angle of particle deflection is limited by the tilted angle of pressure nodes. Therefore, the difference in displacement between particles can actually be reduced at a high acoustic intensity, meaning that a moderate acoustic intensity is needed to achieve optimum separation performance (Fig. S9 in the Supporting Information).

Fig. 3E shows the relationship between particle deflection and particle size (2, 4.5, 6, and 10 μm). The raw image data can be found in Fig. S8B in the Supporting Information. At the same input power (drive voltage of 23 V_{pp} , or 29.4 dBm) the transverse trajectories of the four different particles can be differentiated when exiting the acoustic fields. This is in good agreement with the fact that in Equations (1) and (2), the acoustic radiation force increases proportionally to the volume (r^3) of the particle, but the Stokes drag force increases proportionally to the radius of particle (r). As a result, particles with a larger size move closer to the tilted-angle pressure node, while particles with a smaller size do not have enough net force to move to the pressure node, as shown in Fig. 3B. Fig. 3F shows the relationship between particle volume ratio and deflection displacement difference. Here, 2 μm particles were selected as the base, and compared to 10, 6, and 4.5 μm particles, respectively. Based on Equation (1), a larger particle volume ratio should lead to a larger difference in acoustic radiation force, and thus a larger difference in deflection displacement. This reasoning is in good agreement with the result in Fig. 3F, demonstrating the excellent controllability and sensitivity of our disposable acoustofluidic chips. Our device's controllability enables the deflection of a single stream

of particles, while its sensitivity allows the precise size-based differentiation while using a single frequency in a single device.

them from the original mixture. Fig. 4C provides scanning electron microscope (SEM) images of the original and separated samples. At

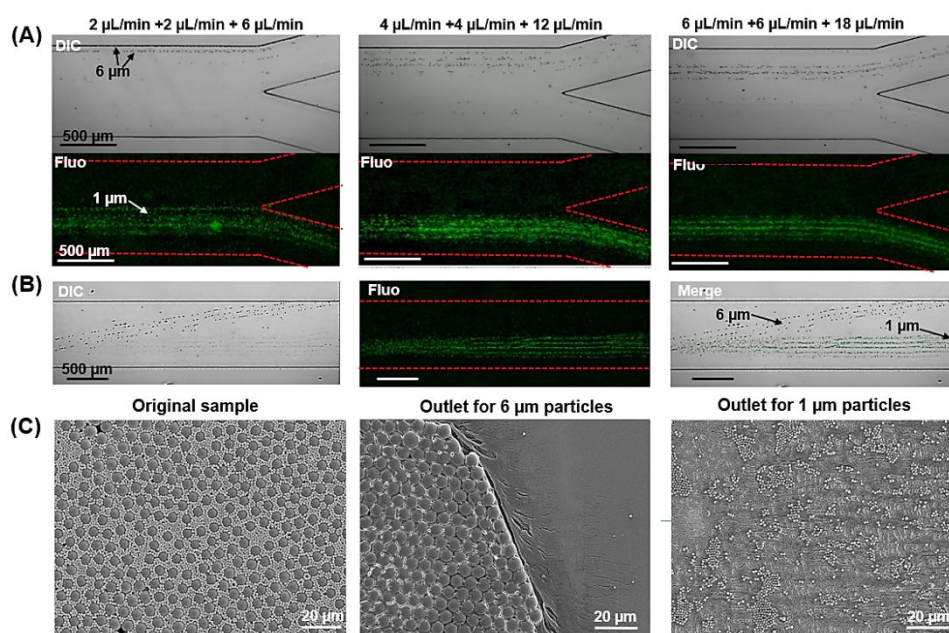


Fig. 4 The taSSAW field in disposable acoustofluidic chips for the separation of 1 μm fluorescent particles and 6 μm non-fluorescent PS particles. (A) High-performance separation was maintained despite the increased throughput. 2+2+6 $\mu\text{L}/\text{min}$: the flow rates of the sample and the two sheath fluids were 2, 2, and 6 $\mu\text{L}/\text{min}$, respectively. (B) Bright-field, fluorescent, and merged images within the acoustic working region. The flow rates of the sample and the two sheath fluids were 2, 2, and 6 $\mu\text{L}/\text{min}$, respectively. (C) SEM images showing the sample before (the mixture of 1 and 6 μm particles) and after acoustic separation (collected from two outlets of the disposable microchannel).

Disposable acoustofluidic chips for nano/micro particle separation

After exploring the dependence of particle deflection on acoustic intensity and particle size, we demonstrated the separation of 1 μm and 6 μm particles in a continuous flow, as shown in Fig. 4. Here, the diameters of 1 and 6 μm particles are approximately equivalent to that of *E. coli* and human RBCs, respectively.^{3, 66} Thus, these particle sizes will provide insight into our upcoming bacteria and RBC separation experiments. The separation performance was evaluated using the fluorescent and stacked bright-field images at the outlet region. Fig. 4A shows the separation performance between 1 and 6 μm particles at different flow rates. The flow rate of the first sheath flow for sample focusing is the same as the sample flow rate, while the second sheath flow for sample transfer is three times the sample flow rate. For example, 2, 2, and 6 $\mu\text{L}/\text{min}$ were used for the sample, first and second sheath flows, respectively. At the same time, the acoustic intensity was optimized to maintain enough lateral displacement for 6 μm particles. Specifically, the drive voltage is 22.8 V_{pp} (29.3 dBm) at the sample flow rate of 2 and 4 $\mu\text{L}/\text{min}$, but 29.1 V_{pp} (31.4 dBm) at the sample flow rate of 6 $\mu\text{L}/\text{min}$. Overall, the deflection of 6 μm particles caused by the acoustic radiation force decreased with increasing sample flow rate. Despite this decrease, most of 6 μm particles were still driven to the upper outlet and successfully separated from 1 μm particles at the sample flow rate of 6 $\mu\text{L}/\text{min}$ (Video S1 and 2 in the Supporting Information). Some 1 μm particles were also deflected, but this slight deflection did not push the 1 μm particles far enough, and the majority of them still exited through the bottom outlet. Fig. 4B displays the images in the working region of the disposable acoustofluidic device. The acoustic radiation force pushed 6 μm particles along the pressure nodes and separated

a sample flow rate of 2 $\mu\text{L}/\text{min}$, 50 μL of each solution was collected, concentrated, and then went through SEM. In the original sample, a uniform mixture of 1 and 6 μm particles was observed. After separation, only a few 1 μm particles were found in the outlet for the separated 6 μm particle specimen, while 6 μm particles are absent in the 1 μm particles specimen, indicating an effective separation.

With the disposable acoustofluidic device, separation of nano-to-micro particles with small size differences and small particle size (*i.e.*, nanoscale) also becomes feasible. We demonstrate the efficient separation of 110 nm PS and 200 nm Ag particles, 400 nm PS and 660 nm SiO_2 particles, 110 nm and 1 μm PS particles, 1 μm and 4.5 μm PS particles, 2 μm and 4.5 μm PS particles, 2 μm and 6 μm PS particles, and 6 and 10 μm PS particles. According to the influence of acoustic intensity on particle separation, the drive voltage was optimized as 35.2 V_{pp} (33.1 dBm) for 1 μm PS, 200 nm Ag, and 660 nm SiO_2 separation, but 24.9 V_{pp} (30.1 dBm) for 4.5 μm PS separation. In Fig. 5A, in different scenarios, the large particles, which were subjected to a large acoustic radiation force, have been deflected away from the small particles. Meanwhile, small particles remained in the sample stream and exited microchannel through the bottom outlet. With the disposable device, we first demonstrated the size-based PS microparticle separation, with a very small size down to 200 nm, with a very small size difference in 2 μm and 4.5 μm , and with a very small size ratio in 6 and 10 μm (Fig. 5A and Fig. S10 in the Supporting Information). We then showed the nanoparticle separation for 110 nm PS particles and 200 nm Ag particles, 400 nm PS particles and 660 nm SiO_2 particles (Figs. 5A and B). To achieve favorable separation performance, the flow rate of sample and two sheath fluids for nanoparticle separation was tuned to 2, 2, and 5 $\mu\text{L}/\text{min}$,

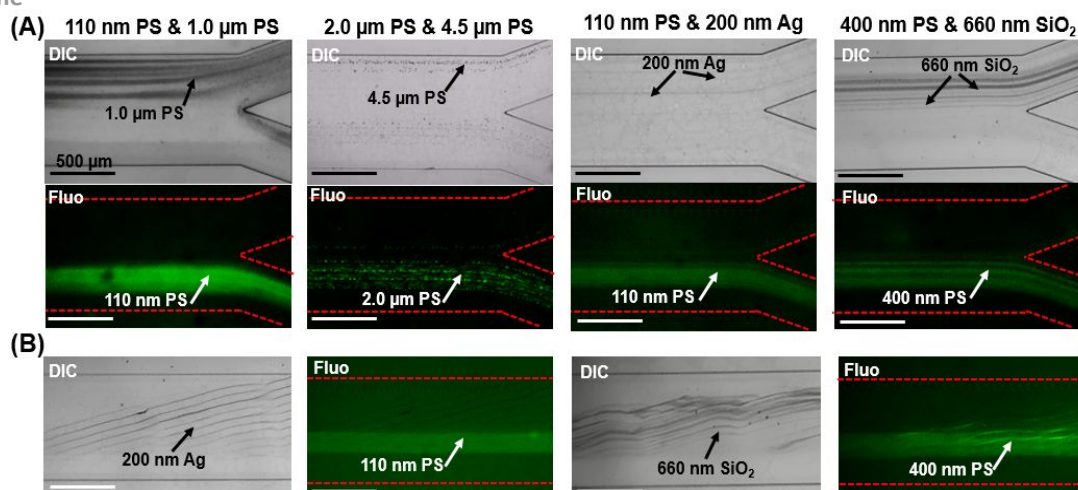


Fig. 5 Disposable acoustofluidic chips for nano/micro particle separation in a continuous flow. (A) Bright-field and fluorescent images at the outlet region for different mixtures of dissimilarly sized particles. These combinations are shown from left to right as 110 nm and 1.0 μm PS particles, 2.0 μm and 4.5 μm PS particles, 110 nm PS particles and 200 nm Ag particles, and 400 nm PS particles and 660 nm SiO₂ particles. (B) Bright-field, fluorescent, and merged images within the acoustic working region for the separation of 110 nm PS particles from 200 nm Ag particles, and 400 nm PS particles from 660 nm SiO₂ particles.

respectively. The large acoustic radiation force experienced by the 200 nm Ag and 660 nm SiO₂ nanoparticles, resulting from their significantly larger acoustic contrast factor relative to PS particles (ϕ is 0.437 for PS, 2.295 for Ag and 1.786 for SiO₂),⁶⁷ pushes Ag and SiO₂ nanoparticles toward the tilted-angle pressure node, and separates them from PS nanoparticles. In previous SAW devices for nanoparticle separation, researchers directly placed IDTs under the microchannel, or employed a Bragg reflector to improve the acoustic radiation force,^{68, 69} our device differs from these previous designs in that we enhance the acoustic radiation force by generating SSAWs from two identical unidirectional transducers. Video S3 and Video S4 in the Supporting Information show the separation process for 400 nm PS particles and 660 nm SiO₂ particles.

Disposable acoustofluidic chips for bacteria separation

To further demonstrate its capability for purification of biological samples, our disposable acoustofluidic chips were used to separate *E. coli* bacteria from human RBCs in phosphate buffered saline (PBS). The capability of separating bacteria from human blood cells would

promise rapid diagnosis in blood related diseases such as sepsis.^{3, 5, 66} In order to observe the *E. coli* bacteria clearly, they were stained with a live/dead BacLight kit (L7007, Invitrogen, USA).⁷⁰ Accordingly, images of the live bacteria with green fluorescence were recorded. Fig. 6A shows the bright-field and fluorescence images for RBCs and *E. coli*, respectively. When exposed to the taSSAW field at 25.6 V_{PP} (30.3 dBm), the majority of the RBCs were pushed away from the bottom outlet to the upper outlet. Specifically, an acoustics on-off-on process was recorded to show the movement trajectories of RBCs (Video S5 in the Supporting Information). In comparison, even with the acoustic signal on, *E. coli* continued to exit the channel through the sample stream (right image in Fig. 6A and Video S6 in the Supporting Information), demonstrating an excellent separation from RBCs. We further characterized the performance of bacteria separation using a flow cytometer. Fig. 6B shows the flow cytometry results of the original mixture, the separated *E. coli*, and the separated RBCs. In the plot of forward scatter (FSC) and side scatter (SSC) (Fig. 6B), *E. coli* and RBCs populations can be distinguished easily due to their large size difference. For the original sample, the ratios of RBCs and *E. coli* to the total number of cells were 69.3% and

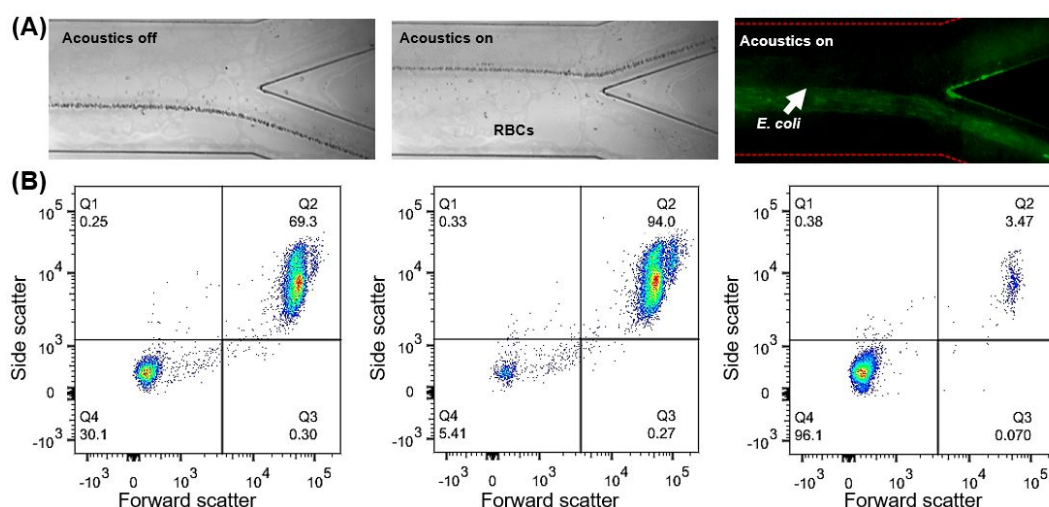


Fig. 6 (A) Bright-field and fluorescent images for bacteria separation via the disposable acoustofluidic chip. (B) Flow cytometry results of the *E. coli* and RBCs mixture, the separated *E. coli*, and the separated RBCs.

30.1%, respectively. After separation, this ratio for the RBCs increased to 94.0% in the top outlet collection, while it increased to 96.1% for *E. coli* in the bottom outlet collection. The viability of bacteria was also measured as 99.8% before SAW separation and 97.5% after SAW separation, showing good biocompatibility of our disposable acoustofluidic devices (Fig. S11 in the Supporting Information). In previous research, Ai. et al. separated peripheral blood mononuclear cells (PBMCs) from *E. coli* with a purity of 95.65% using a permanently bonded SAW device, where the concentration of *E. coli* and PBMCs were both approximately 3×10^6 particles/mL.³⁹ These results indicate that our disposable acoustofluidic device can achieve comparable cell/bacteria separation performance relative to the permanently bonded SAW devices, validating its potential for future real-world applications.

Conclusions

In this work, we developed a disposable acoustofluidic platform by assembling a disposable microchannel onto a reusable piezoelectric substrate coated with IDTs. A pair of unidirectionally distributed IDTs was designed to generate a strong taSSAW field. To improve acoustic energy transmission, a hybrid hard/soft PDMS channel design was employed, in which a hard PDMS film with a thin thickness and a low acoustic attenuation factor was used as the microchannel bottom enclosure. We then demonstrated a strong taSSAW acoustic field within disposable microchannels by concentrating 400 nm PS particles along tilted-angle pressure nodes. Particle velocity measurements also reveal that the intensity of acoustic radiation force achieved in our disposable acoustofluidic chips is comparable to that in devices with permanently bonded channels. The ability to distinguish the deflection distances of four different sized particles indicates the favorable controllability and sensitivity of our disposable devices.

For particle separation, our unidirectional IDT-based disposable acoustofluidic chips can separate nano-to-micro particles, and also differentiate bacteria from human RBCs. We demonstrated that particles with a wide size range from 200 nm to 10 μ m can be separated. For example, the separation of 2 and 4.5 μ m PS particles with relatively small size difference indicates the accuracy and sensitivity of our disposable devices. And the separation of 200 nm Ag particles from 110 nm PS particles and 660 nm SiO₂ particles from 400 nm PS particles suggest the capability of our disposable device for nanoparticle separation. Additionally, an efficiency up to 96% was achieved for bacteria and human RBCs separation. With its features of being biocompatible, label-free, efficient, versatile, and cost-effective, this technology would significantly expedite the implementation of acoustic separation systems into practical biomedical and clinical applications, such as cell phenotyping, sample purification, cell and bacteria separation.

Author contributions

S. Z., and T. J. H. designed the research. S. Z. fabricated devices, conducted experiments, and prepared the manuscript. S. Z., M. W., S. Y., and Y. G., analyzed the data. C.C. and J.X. conducted the numerical simulations. Y. W. and J. Y. helped with the particle

velocity measurement. Z. T., H. B., and P. H. edited the manuscript. X. Z., and H. Z. drew the schematic figure. S. Y., and P. Z. helped with the hybrid microchannel fabrication. T. J. H. supervised the work and edited the manuscript.

Conflicts of interest

T.J.H. has co-founded a start-up company, Ascent Bio-NanoTechnologies Inc., to commercialize technologies involving acoustofluidics and acoustic tweezers.

Acknowledgements

We thank Prof. Liying Zhang for kindly providing us the SiO₂ nanoparticles. We thank the Analytical Instrument Facility (AIF) at North Carolina State University for the measurement of PDMS hardness. We thank Defei Liao and Prof. Pei Zhong for the support in measuring the acoustic performance of PDMS materials. The authors gratefully acknowledge financial support from the National Institutes of Health (UG3TR002978, R01GM135486, R01HD086325, R44GM125439, R43HL140800, and R43AG063643) and the United States Army Medical Research Acquisition Activity (W81XWH-18-1-0242). Shuaiguo Zhao acknowledges the financial support from the China Scholarship Council.

References

- B. H. Wunsch, J. T. Smith, S. M. Gifford, C. Wang, M. Brink, R. L. Bruce, R. H. Austin, G. Stolovitzky and Y. Astier, *Nat. Nanotechnol.*, 2016, **11**, 936-940.
- M. Wu, Y. Ouyang, Z. Wang, R. Zhang, P.-H. Huang, C. Chen, H. Li, P. Li, D. Quinn, M. Dao, S. Suresh, Y. Sadvovsky and T. J. Huang, *Proc. Natl. Acad. Sci. U. S. A.*, 2017, **114**, 10584-10589.
- Y. Ai, C. K. Sanders and B. L. Marrone, *Anal. Chem.*, 2013, **85**, 9126-9134.
- J.-J. Lee, K. J. Jeong, M. Hashimoto, A. H. Kwon, A. Rwei, S. A. Shankarappa, J. H. Tsui and D. S. Kohane, *Nano Lett.*, 2013, **14**, 1-5.
- P. Dow, K. Kotz, S. Gruszka, J. Holder and J. Fiering, *Lab Chip*, 2018, **18**, 923-932.
- X. Ding, Z. Peng, S.-C. S. Lin, M. Geri, S. Li, P. Li, Y. Chen, M. Dao, S. Suresh and T. J. Huang, *Proc. Natl. Acad. Sci. U. S. A.*, 2014, **111**, 12992-12997.
- W. Zhao, T. Zhu, R. Cheng, Y. Liu, J. He, H. Qiu, L. Wang, T. Nagy, T. D. Querec and E. R. Unger, *Adv. Funct. Mater.*, 2016, **26**, 3990-3998.
- M. Wu, Z. Mao, K. Chen, H. Bachman, Y. Chen, J. Rufo, L. Ren, P. Li, L. Wang and T. J. Huang, *Adv. Funct. Mater.*, 2017, **27**, 1606039.
- P. Li and T. J. Huang, *Anal. Chem.*, 2018, **91**, 757-767.
- H. Ahmed, G. Destgeer, J. Park, J. H. Jung and H. J. Sung, *Adv. Sci.*, 2018, **5**, 1700285.
- M. Aghaamoo, A. Aghilinejad, X. Chen and J. Xu, *Electrophoresis*, 2019, **40**, 1486-1493.
- A. Ozcelik, J. Rufo, F. Guo, Y. Gu, P. Li, J. Lata and T. J. Huang, *Nat. Methods*, 2018, **15**, 1021-1028.
- S. M. Friedrich, R. Bang, A. Li and T.-H. Wang, *Anal. Chem.*, 2019, **91**, 2822-2830.
- M. P. MacDonald, G. C. Spalding and K. Dholakia, *Nature*, 2003, **426**, 421-424.
- B. Kang, J. Shin, H.-J. Park, C. Rhyou, D. Kang, S.-J. Lee, Y.-s. Yoon, S.-W. Cho and H. Lee, *Nat. Commun.*, 2018, **9**, 5402.
- L. Schmid, D. A. Weitz and T. Franke, *Lab Chip*, 2014, **14**, 3710-3718.
- J. Reboud, Y. Bourquin, R. Wilson, G. S. Pall, M. Jiwaji, A. R. Pitt, A. Graham, A. P. Waters and J. M. Cooper, *Proc. Natl. Acad. Sci. U. S. A.*, 2012, **109**, 15162-15167.
- R. J. Shilton, M. Travaglini, F. Beltram and M. Cecchini, *Adv. Mater.*, 2014, **26**, 4941-4946.
- M. Miansari and J. R. Friend, *Adv. Funct. Mater.*, 2016, **26**, 7861-7872.
- Y. Bourquin, R. Wilson, Y. Zhang, J. Reboud and J. M. Cooper, *Adv. Mater.*, 2011, **23**, 1458-1462.

21. S. P. Zhang, J. Lata, C. Chen, J. Mai, F. Guo, Z. Tian, L. Ren, Z. Mao, P.-H. Huang, P. Li, S. Yang and T. J. Huang, *Nat. Commun.*, 2018, **9**, 2928.
22. D. J. Collins, B. Morahan, J. Garcia-Bustos, C. Doerig, M. Plebanski and A. Neild, *Nat. Commun.*, 2015, **6**, 8686.
23. H. Ahmed, A. R. Rezk, B. J. Carey, Y. Wang, M. Mohiuddin, K. J. Berean, S. P. Russo, K. Kalantar-zadeh and L. Y. Yeo, *Adv. Mater.*, 2018, **30**, 1704756.
24. F. Guo, Z. Mao, Y. Chen, Z. Xie, J. P. Lata, P. Li, L. Ren, J. Liu, J. Yang and M. Dao, *Proc. Natl. Acad. Sci. U. S. A.*, 2016, **113**, 1522-1527.
25. W.-K. Cao, L.-T. Wu, C. Zhang, J.-C. Ke, Q. Cheng, T.-J. Cui and Y. Jing, *Sci. Bull.*, 2019, **64**, 808-813.
26. D. J. Collins, C. Devendran, Z. Ma, J. W. Ng, A. Neild and Y. Ai, *Sci. Adv.*, 2016, **2**, e1600089.
27. K. Mutafooulos, P. Spink, C. Lofstrom, P. Lu, H. Lu, J. Sharpe, T. Franke and D. Weitz, *Lab Chip*, 2019, **19**, 2435-2443.
28. V. Skowronek, R. W. Rambach, L. Schmid, K. Haase and T. Franke, *Anal. Chem.*, 2013, **85**, 9955-9959.
29. K. Lee, H. Shao, R. Weissleder and H. Lee, *ACS Nano*, 2015, **9**, 2321-2327.
30. H. Ahmed, G. Destgeer, J. Park, M. Afzal and H. J. Sung, *Anal. Chem.*, 2018, **90**, 8546-8552.
31. P. Li, Z. Mao, Z. Peng, L. Zhou, Y. Chen, P.-H. Huang, C. I. Truica, J. J. Drabick, W. S. El-Deiry, M. Dao, S. Suresh and T. J. Huang, *Proc. Natl. Acad. Sci. U. S. A.*, 2015, **112**, 4970-4975.
32. Z. Tian, S. Yang, P.-H. Huang, Z. Wang, P. Zhang, Y. Gu, H. Bachman, C. Chen, M. Wu and Y. Xie, *Sci. Adv.*, 2019, **5**, eaau6062.
33. Z. Mao, P. Li, M. Wu, H. Bachman, N. Mesyngier, X. Guo, S. Liu, F. Costanzo and T. J. Huang, *ACS Nano*, 2017, **11**, 603-612.
34. J. Park, J. H. Jung, K. Park, G. Destgeer, H. Ahmed, R. Ahmad and H. J. Sung, *Lab Chip*, 2018, **18**, 422-432.
35. P. Li, Z. Ma, Y. Zhou, D. J. Collins, Z. Wang and Y. Ai, *Anal. Chem.* 2019, **91**, 9970-9977.
36. J. Park, J. H. Jung, G. Destgeer, H. Ahmed, K. Park and H. J. Sung, *Lab Chip*, 2017, **17**, 1031-1040.
37. F. Guo, Y. Xie, S. Li, J. Lata, L. Ren, Z. Mao, B. Ren, M. Wu, A. Ozcelik and T. J. Huang, *Lab Chip*, 2015, **15**, 4517-4523.
38. C. Witte, J. Reboud, R. Wilson, J. Cooper and S. Neale, *Lab Chip*, 2014, **14**, 4277-4283.
39. Z. Ma, D. J. Collins and Y. Ai, *Anal. Chem.*, 2016, **88**, 5316-5323.
40. K. Olofsson, V. Carannante, M. Ohlin, T. Frisk, K. Kushiuro, M. Takai, A. Lundqvist, B. Önfelt and M. Wiklund, *Lab Chip*, 2018, **18**, 2466-2476.
41. J. Friend and L. Y. Yeo, *Rev. Mod. Phys.*, 2011, **83**, 647-704.
42. M. Wu, C. Chen, Z. Wang, H. Bachman, Y. Ouyang, P.-H. Huang, Y. Sadovsky and T. J. Huang, *Lab Chip*, 2019, **19**, 1174-1182.
43. D. J. Collins, R. O'Rourke, C. Devendran, Z. Ma, J. Han, A. Neild and Y. Ai, *Phys. Rev. Lett.*, 2018, **120**, 074502.
44. L. Tian, N. Martin, P. G. Bassindale, A. J. Patil, M. Li, A. Barnes, B. W. Drinkwater and S. Mann, *Nat. Commun.*, 2016, **7**, 13068.
45. M. Caleap and B. W. Drinkwater, *Proc. Natl. Acad. Sci. U. S. A.*, 2014, **111**, 6226-6230.
46. K. Xu, C. P. Clark, B. L. Poe, J. A. Lounsbury, J. Nilsson, T. Laurell and J. P. Landers, *Anal. Chem.*, 2019, **91**, 2186-2191.
47. K. Cushing, E. Undvall, Y. Ceder, H. Lilja and T. Laurell, *Anal. Chim. Acta*, 2018, **1000**, 256-264.
48. H. Ahmed, L. Lee, C. Darmanin and L. Y. Yeo, *Adv. Mater.*, 2018, **30**, 1602040.
49. T.-Y. Lin, T. Do, P. Kwon and P. B. Lillehoj, *Lab Chip*, 2017, **17**, 241-247.
50. Y. Lin, Y. Gao, M. Wu, R. Zhou, D. Chung, G. Caraveo and J. Xu, *Lab Chip*, 2019, **19**, 3045-3053.
51. P. B. Lillehoj, F. Wei and C.-M. Ho, *Lab Chip*, 2010, **10**, 2265-2270.
52. M. Mauk, J. Song, H. H. Bau, R. Gross, F. D. Bushman, R. G. Collman and C. Liu, *Lab Chip*, 2017, **17**, 382-394.
53. C. Liu, J. A. Thompson and H. H. Bau, *Lab Chip*, 2011, **11**, 1688-1693.
54. U. S. Jonnalagadda, M. Hill, W. Messaoudi, R. B. Cook, R. O. Oreffo, P. Glynn-Jones and R. S. Tare, *Lab Chip*, 2018, **18**, 473-485.
55. P. H. Huang, S. Zhao, H. Bachman, N. Nama, Z. Li, C. Chen, S. Yang, M. Wu, S. P. Zhang and T. J. Huang, *Adv. Sci.*, 2019, 1900913.
56. M. Wu, A. Ozcelik, J. Rufo, Z. Wang, R. Fang and T. J. Huang, *Microsynt. Nanoeng.*, 2019, **5**, 32.
57. Y. Xie, H. Bachman and T. J. Huang, *TrAC, Trends Anal. Chem.*, 2019, **117**, 280-290.
58. H. Schmid and B. Michel, *Macromolecules*, 2000, **33**, 3042-3049.
59. W. He, L. Huang, Y. Feng, F. Liang, W. Ding and W. Wang, *Biomicrofluidics*, 2019, **13**, 054109.
60. J. K. Tsou, J. Liu, A. I. Barakat and M. F. Insana, *Ultrasound Med. Biol.*, 2008, **34**, 963-972.
61. A. Thouvenot, T. Poepping, T. M. Peters and E. C. Chen, *International Society for Optics and Photonics*, 2016, 97835E.
62. K. Anwar, T. Han and S. M. Kim, *Sensors Actuators B: Chem.*, 2011, **153**, 301-311.
63. K. Melde, E. Choi, Z. Wu, S. Palagi, T. Qiu and P. Fischer, *Adv. Mater.*, 2018, **30**, 1704507.
64. M. Wu, P. H. Huang, R. Zhang, Z. Mao, C. Chen, G. Kemeny, P. Li, A. V. Lee, R. Gyanchandani and A. J. Armstrong, M. Dao, S. Suresh, and T. J. Huang, *Small*, 2018, **14**, 1801131.
65. A. Fakhfour, C. Devendran, T. Albrecht, D. J. Collins, A. Winkler, H. Schmidt and A. Neild, *Lab Chip*, 2018, **18**, 2214-2224.
66. S. Li, F. Ma, H. Bachman, C. E. Cameron, X. Zeng and T. J. Huang, *J. Micromech. Microeng.*, 2016, **27**, 015031.
67. J. T. Karlsen and H. Bruus, *Phys. Rev. E*, 2015, **92**, 043010.
68. P. Sehgal and B. J. Kirby, *Anal. Chem.*, 2017, **89**, 12192-12200.
69. D. J. Collins, T. Alan and A. Neild, *Lab Chip*, 2014, **14**, 1595-1603.
70. S. Zhao, W. He, Z. Ma, P. Liu, P.-H. Huang, H. Bachman, L. Wang, S. Yang, Z. Tian, Z. Wang, Y. Gu, and Z. Xie, and T. Huang, *Lab Chip*, 2019, **19**, 941-947.